



# Advancing Nozzle Contour Design: A Numerical-Experimental Comparison and Optimization of Hypersonic Flow Characteristics

Daniel Maurat<sup>1</sup>, Gabriel Axtmann<sup>1</sup>, Uwe Gaisbauer<sup>1</sup>, Robert Hruschka<sup>2</sup>, Friedrich Leopold<sup>2</sup>

## **Abstract**

Hypersonic test facilities are used to accelerate the fluid to the desired test conditions. Hypersonic nozzles are classically designed by using the Method of Characteristics (MoC) in combination with a boundary layer correction. However, previous studies has shown that this design method is only valid for design Mach numbers below eight, since it assumes a boundary layer that remains relatively thin compared to the nozzle radius. This assumption is no longer valid for higher Mach numbers.

An alternative approach to overcome this limitation is the design-by-analysis method, which uses the results from numerical simulations of the nozzle flow to generate the nozzle contour at the desired design point. For this purpose, the framework HyNCO (Hypersonic Nozzle Contour Optimization) has been developed at the Institute for Aerodynamics and Gas Dynamics, University of Stuttgart (IAG), combining numerical simulations with a multi-objective genetic optimization approach to generate a group of optimized nozzle contours.

To obtain accurate and reliable results, selecting the appropriate numerical setup is crucial. The choice of gas model significantly influences the simulation's precision and computational efficiency. Therefore, a numerical study has been conducted consisting of three cases: thermally and calorically perfect gas with a range of constant isentropic exponents, real gas as one species with an temperature dependent isentropic exponent and a gas in thermochemical non-equilibrium. These results were compared with experimental results obtained at the STB shock tunnel at French-German Research Institute of Saint-Louis (ISL) for a nozzle with exit Mach number of  $M_{\rm e}=8$ .

Among the numerical cases, the thermochemical non-equilibrium model provided the closest reproduction of the experimental results. However, its high computational effort makes it impractical for the optimization process. On the other hand, the case using a constant isentropic exponent also agrees well with the experimental data while requiring significantly less computational effort. It is therefore the preferred choice for nozzle optimization.

Based on this study, a nozzle contour optimization with HyNCO for the Mach 8 nozzle at the STB shock tunnel is conducted. In addition to the nozzle flow, the thermal and mechanical loads on the nozzle are evaluated with regards to the possibility of modular nozzles and different materials for the nozzle wall.

**Keywords:** Nozzle, Optimization, Non-equilibrium, Shock tunnel, Hypersonics, Experimental Investigation, Numerical Investigation, Comparison, Validation

#### **Nomenclature**

HiSST-2025-0057 Page | 1

<sup>&</sup>lt;sup>1</sup>University of Stuttgart, Institute for Aerodynamics and Gasdynamics, Stuttgart, Germany

<sup>&</sup>lt;sup>2</sup>French-German Research Institue of Saint-Louis, Saint-Louis, France

 $p_{Pitot}$  – Pitot pressure

q – Heat flux

r - Radius

u, v, w – Velocity components in x, y and z direc-

tions

x, y, z - Spatial directions

 $y^+$  – Dimensionless wall distance

Greek

 $\Phi$  – Flow angle

 $\gamma$  – Isentropic exponent  $\delta^*$  – Displacement thickness

 $\omega$  - Nozzle wall inflection point angle

 $\omega$  – Weighting coefficient

Subscripts

0 - Stagnation conditions

ax – Axial

e – Nozzle exit

inv - Inviscid

noz – Nozzle

tgt - Target value

 $\it th$  – Throat

 $v\,$  – Vibrational

visc – Viscous

w – Wall

#### 1. Introduction

The renewed interest in hypersonic flows necessitates the ability to investigate such flows under a variety of conditions. A key aspect of this is the conduct of experimental investigations to validate both numerical and analytical models. Examples of such facilities include the STA and STB shock tubes at the French-German Research Institute of Saint-Louis (ISL), which can operate at Mach numbers between 3 and 10 [1]. To achieve this, a nozzle is utilized.

The conventional approach to nozzle design involves the application of the Method of Characteristics (MoC), developed by Prandtl and Busemann in the 1920s [2]. Initially developed as a graphical design method for inviscid, two-dimensional (2D) nozzles, it has been refined over the decades, for instance, for axisymmetric nozzles [3]. However, nozzles designed using the MoC do not account for viscous effects, particularly the boundary layer developing along the nozzle wall. To address this limitation, the MoC was extended to include a boundary layer correction (MoC/BL) [4], in which the displacement thickness  $\delta^*$  is added to the inviscid nozzle contour. This approach assumes that the boundary layer is small compared with the local nozzle radius and that the characteristic lines reflect at the displacement thickness.

With the advent of Computational Fluid Dynamics (CFD) in the latter half of the 20th century, it became possible to investigate nozzle flows in greater detail and to account for thermochemical non-equilibrium effects. In the early 1990s, CFD was used to assess the limitations of MoC/BL. Benton and Perkins [5] and Candler and Perkins [6] showed that for nozzles designed with  $M_{e,{\rm design}}>8$ , the MoC/BL method becomes unreliable because the boundary layer thickness constitutes a significant fraction of the nozzle radius. Consequently, the characteristic lines penetrate the displacement thickness and reflect closer to the wall than expected.

# 2. Methodology

# 2.1. Nozzle Contour Design

Due to the limitations of the Method of Characteristics, several alternative design approaches have been developed. One such approach is the Design-by-Analysis method [7], which employs numerical simulations to derive the desired nozzle contour. Originally proposed by Korte et al. [8], this approach led to the development of the CAN-DO design program. CAN-DO evaluates the results of two-dimensional (2D) or axisymmetric numerical simulations and iteratively adjusts a parameterized nozzle contour.

The program assesses three objective functions, Obj(X), which serve as measures of nozzle performance and depend on the design parameters X. These functions are based on the exit Mach number  $M_e$ , the exit flow angle  $\Phi_e = \arctan\left(\frac{v_e}{u_e}\right)$ , and the centreline Mach number distribution  $M_{ax}$ . While the target values of  $M_e$  and  $\Phi_e$  are set as constants, the centreline Mach number distribution is determined for each nozzle using the method of Sivells [4], as it depends on the nozzle contour.

The nozzle contour itself is represented using N cubic splines. The spline coefficients constitute the design parameter space, which can be reduced to N+3 coefficients by enforcing slope and curvature continuity between splines [8]. Nevertheless, alternative spline formulations may also be employed. For instance, Bézier splines [9] define the parameter space through Bézier control points, while B-splines [10] use basis function coefficients. For a spline of degree d, both formulations require 2(d+1)

design parameters.

Whereas CAN-DO applies a least-squares optimization procedure, nozzle contours can alternatively be obtained using multi-objective genetic algorithms (MOGA) [11], as demonstrated by Matsunaga et al. [9]. In this method, a population of candidate solutions is randomly generated from the design parameter space and evaluated against the chosen objective functions. Successive populations are then formed through crossover of parent solutions and mutation of offspring. This evolutionary process is repeated over a prescribed number of generations. In comparison to single-objective optimization, this approach allows the user to choose a result from a family of results if no global minimum exists.

The concepts described above are integrated into the framework *HyNCO* (Hypersonic Nozzle Contour Optimization). Within this framework, numerical simulations are performed using the open-source toolkit *OpenFOAM* [12], specifically with the *HiSA* extension [13], while optimization is managed through the open-source library *Dakota* [14]. The workflow of the framework is shown in Fig 1, and it is currently capable of designing both two-dimensional and axisymmetric nozzles.

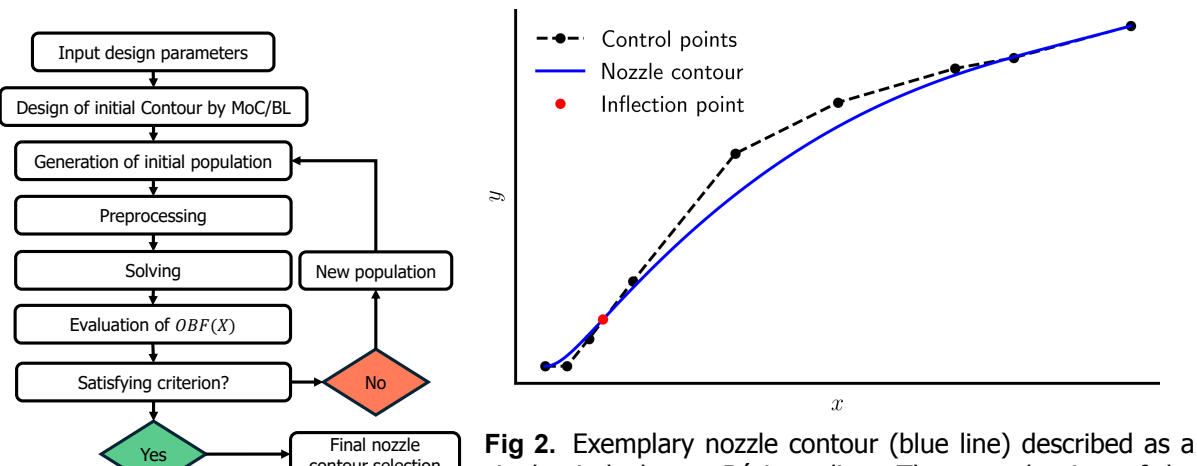


Fig 1. Flowchart for HyNCO

single eigth degree Bézier spline. The control points of the spline are shown as black dots, the inflection point of the contour is marked as a red dot.

The initial nozzle contour is generated using the MoC design tool Contur [15] and subsequently fitted to a Bézier curve of degree N, specified by the user. The design parameters for the optimization are defined as the differences between neighbouring control points together with the throat radius, which initially results in 2(N+1) design parameters.

This number is reduced by imposing constraints on the wall angle and curvature at both the throat and the nozzle exit, with the throat wall curvature optionally constrained as well. At the throat, the wall angle is fixed at zero and the curvature is defined as a multiple of the throat radius, which also serves as an input variable for the calculation of the axial Mach number distribution. At the nozzle exit, the wall angle remains a design parameter while the curvature is set to zero. Applying these constraints reduces the parameter space to 2N-3 design parameters describing the nozzle contour.

An exemplary nozzle contour with its control points and design parameters is shown in Fig 2. Based on these parameters and the user-defined bounds, the optimizer generates the initial nozzle population, which is pre-processed and run by the numerical solver. The data for the objective functions is then extracted from the results and transferred back to the optimizer for evaluation.

Similar to the CAN-DO code developed by Korte, the Mach number  $M_e$  and the flow angle  $\Phi_e$  at the nozzle exit, as well as the axial Mach number distribution  $M_{ax}$ , are defined as the primary design targets. Additional targets, such as the radius of the inviscid flow at the nozzle exit  $r_{inv,e}$  or the nozzle length  $l_{noz}$ , are available but are not considered in the scope of this publication. Each objective function is then calculated as

$$Obj_k(X) = \sum_{j=1}^{n_k} \left[ \omega_{k,j} (f_j - f_{tgt})^2 \right]$$
 (1)

with the individual weighting coefficient [16]

$$\omega_{k,j} = \frac{\exp(-|f_j - f_{tgt}|)}{\sum_{j=1}^{n_k} \exp(-|f_j - f_{tgt}|)}.$$
 (2)

For  $M_e$  and  $\Phi_e$ , only the core flow at the nozzle exit is used in determining the objective function values. Therefore, the boundary layer thickness is determined and subtracted from the viscous contour. For  $M_{ax}$ , the inviscid contour provides the necessary input parameters, such as the wall angle at the inflection points  $\theta$  and the ratio of the throat radius to the radius of curvature at the throat,

$$R = \frac{r_{th}}{r_{curv.th}}. (3)$$

The design Mach number  $M_{e,design}$  and the isentropic ratio  $\gamma$  are also required. The axial Mach number distribution is divided into four regions: (i) between the throat and the inflection point, a fourth-degree polynomial describes the Mach number, (ii) the region close to the inflection point is assumed to be radial, (iii) a fifth-degree polynomial is used to model the Mach number distribution, (iv): uniform flow at the design Mach number is assumed. These regions are illustrated in Fig 3. For a detailed description of the Mach number curve, refer to the original work by Sivells [4].

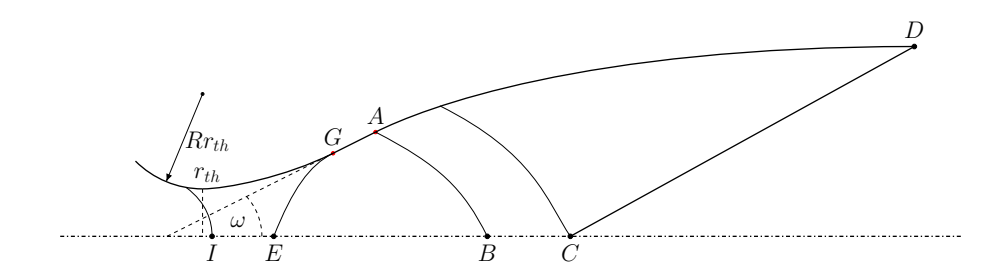


**Fig 3.** Nozzle flow regions for the determination of centreline Mach number distribution. According to Sivells [4]

#### Thermochemical Non-Equilibirum Flow

For hypersonic flows, the usual assumption of a perfect gas in thermochemical equilibrium with a constant isentropic exponent  $\gamma$  is no longer valid. To illustrate this, Fig 4 shows the different mechanisms of excitation, dissociation, and ionization of air as a function of temperature.

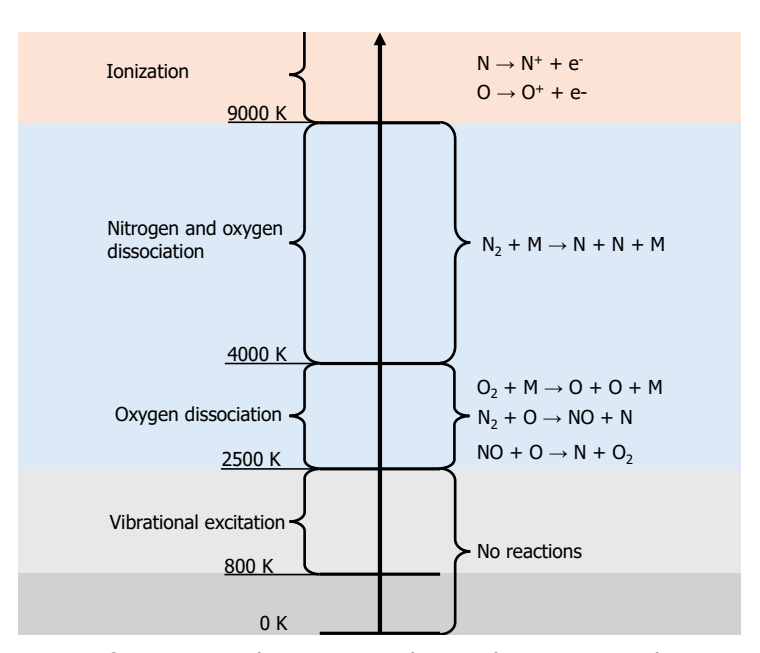


Fig 4. Temperature ranges of excitation, dissociation, chemical reactions and ionization for Air. According to Zhang et al. [17].

For example, if a vehicle is flown at a Mach number of M=8 in the atmosphere at a height of  $H=30\,\mathrm{km}$ , the atmospheric temperature and pressure are  $T=227\,\mathrm{K}$  and  $p=1172\,\mathrm{Pa}$ , respectively [18]. Calculating the stagnation conditions using the isentropic relation with an assumed  $\gamma = 1.4$ yields a temperature of  $T_0 = 3128 \,\mathrm{K}$  and a pressure of  $p_0 = 114 \,\mathrm{bar}$ . At this temperature, compared to the range in Fig 4, the gas is vibrationally excited and oxygen dissociation has begun, which alters the gas properties and must be considered in numerical simulations. For nozzle flows, the rapid expansion of the gas additionally leads to the freezing of the vibrational energy states [19].

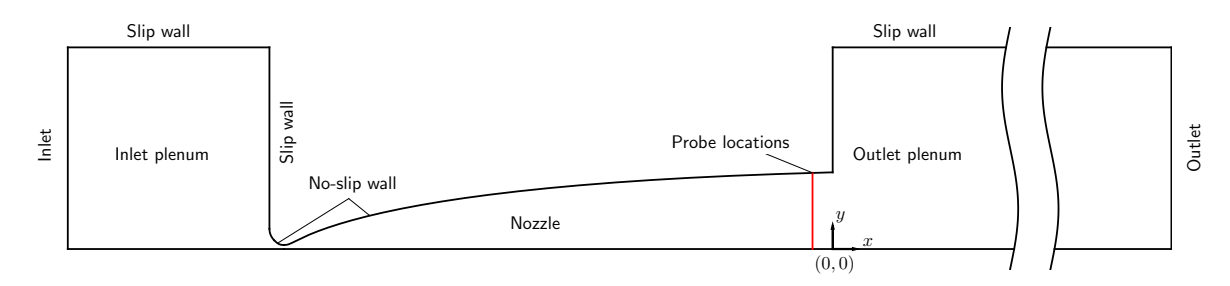
In numerical simulations, the effects of thermodynamic non-equilibrium can be accounted for using the two-temperature model [20], in which the internal energy is split into translational-rotational and vibrational-electronic components. The vibrational-electronic energy, along with the total internal energy, is solved through separate differential equations. The relaxation of the vibrational energy is modeled using the Landau-Teller approach [21]. Such simulations can be carried out with several codes, including hy2Foam, an OpenFOAM extension [22, 23], or Eilmer [24, 25], developed by the University of Queensland.

## 3. Computational Setup

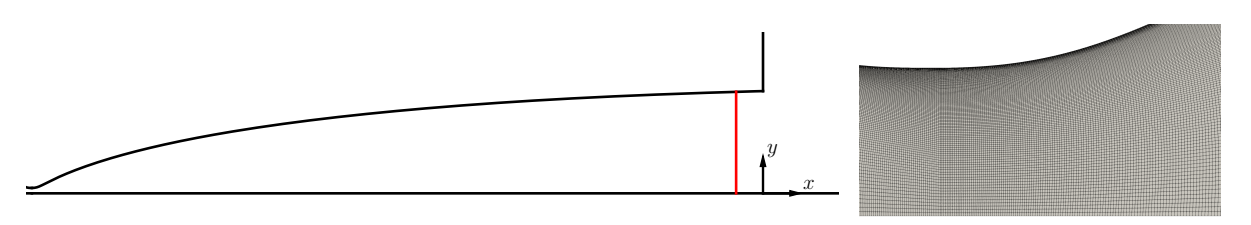
# 3.1. Domain and Spatial Discretization

The computational grid for the flow simulation consists of three major components: the inlet plenum, which provides the total conditions for the nozzle, the nozzle itself, and the outlet plenum. The nozzle considered in this study is the M=8 nozzle from the STB shock tube at ISL [1] and is represented by an eighth-degree Bézier spline. A schematic representation of the domain is shown in Figs. 5a and 5b. The block structured mesh contains 251317 hexahedral cells. The boundary layer consists of 41 points in wall-normal direction with a growth rate of 1.1, see close-up of the mesh in Fig 5c.

HiSST-2025-0057



(a) Schematic view of the computational domain



**(b)** Schematic view of the nozzle with probe positions for the experimental data **(c)** Close-up of the mesh in the marked in red

**Fig 5.** Computational domain for the nozzle simulations. (a): schematic view of the domain; (b): schematic view of nozzle with the position of probes for the experimental data; (c): close-up of the mesh of the throat region

#### 3.2. Numerical Setup

A finite volume, compressible solving algorithm with local time stepping approach is used for achieving a steady state solution. The discretisation in both space and time is second order. As a turbulence model, the Spalart-Allmaras turbulence model [26] with low-Reynolds wall functions ( $y^+ < 5$ ) is used.

With the domain described in Section 3.1, three types of simulations are conducted, differing in two aspects. These are gas model and the simulation code. The first type uses a perfect gas model for nitrogen, in which the isentropic ratio  $\gamma$  differs between each individual simulation. The second type utilizes the Peng-Robinson equation of state [27] with the NIST-JANAF polynomials for modelling the temperature-dependent change in the isobaric heat capacity  $c_p$  [28]. These two types of simulations are run with HiSA [13]. Finally, the third type uses a two-temperature model for thermodynamic non-equilibrium effects in conjunction with a finite rate chemistry solver. This type of simulation is run with Eilmer [24, 25].

#### 3.3. Boundary Conditions

The domain walls are set as slip walls, except for the convergent and divergent nozzle sections, which are modelled as isothermal no-slip walls with a wall temperature of  $T_w=295\,\mathrm{K}$ . The inlet provides the desired total conditions of  $T_0=2650\,\mathrm{K}$  and  $p_0=1.738\times10^7\,\mathrm{Pa}$ , while the outlet in the post-nozzle plenum is defined as a Neumann boundary conditions.

Simulations in thermochemical equilibrium with the perfect gas model are carried out for four specific heat ratios:  $\gamma_1=1.29$ ,  $\gamma_2=1.32$ ,  $\gamma_3=1.36$ , and  $\gamma_4=1.4$ . These values were chosen because  $\gamma_1$  corresponds to nitrogen under total conditions,  $\gamma_4$  is the classical value under standard conditions,  $\gamma_3$  matches the design value of the nozzle, and  $\gamma_2$  is an intermediate value between  $\gamma_1$  and  $\gamma_3$ . The nozzle was originally designed using  $\gamma_3$ .

For the real gas case, the Peng-Robinson equation of state [27] is applied, along with the NIST-JANAF polynomials for the isobaric heat capacity  $c_p$  [28].

The non-equilibrium simulation uses thermally perfect molecular and atomic nitrogen with chemical reaction rates from Park [29] and vibrational-translational relaxation rates from Millikan and White [30]. To validate the numerical results, experimental data from the STB shock tube, obtained using Pitot

probes in the nozzle flow, are employed [1].

## 3.4. Adaptions for Nozzle Contour Optimization

Based on the results of the gas model comparison, a nozzle optimisation is conducted to improve the contour for the specified flow conditions with the HyNCO framework. As the initial quess, the contour of the M=8 STB shock tube nozzle is employed and parametrised as an eighth-degree Bézier spline, resulting in 14 design variables. These comprise seven parameters defining the axial distances between control points, four for the radial distances, as well as the throat radius, throat curvature, and exit wall

Target values for the optimisation are defined as an exit Mach number of  $M_{e,tqt}=8$ , an exit flow angle of  $\Phi_e = 0^{\circ}$ , and a centreline Mach number  $M_{ax}$  estimated using the method of Sivells [4]. Each simulation setup is identical to the above mentioned with the exception of the outlet plenum, which is omitted from the domain to reduce computational costs. The optimisation comprises 5000 individual simulations and requires seven days to complete. Results are compared with the equilibrium case introduced in the previous section, hereafter referred to as the initial case.

## 4. Results

#### 4.1. Influence of Gas Models

The comparison of the numerical and experimental data, shown in Fig 6 for measurements taken 50 mm upstream of the nozzle exit and in Fig 7 along the nozzle axis of symmetry, reveals distinct trends in the equilibrium simulations with constant  $\gamma$ . With increasing  $\gamma$ , the Mach number and Pitot pressure rise, while static pressure, temperature, and velocity decrease. This behavior agrees with the classical isentropic area—Mach number relation, which predicts that for a fixed area ratio between throat and exit, a higher isentropic ratio yields a higher Mach number.

Axial distributions further show an overexpansion of the flow, which becomes more pronounced at higher  $\gamma$ . For instance, in the case of  $\gamma_4=1.4$ , the Mach number increases up to M=10.5 at x=0.55 m but subsequently decreases to  $M_e=9$  at the nozzle exit. This overexpansion and subsequent reduction in Mach number introduce disturbances in the nozzle core flow, visible as a Mach number deficit near the symmetry axis at the nozzle exit. These effects are illustrated in Fig 8.

The primary cause of the observed overexpansion, particularly in the case  $\gamma_4$ , is the mismatch between the nozzle contour and the imposed flow conditions. Specifically, the wall angle at the contour inflection point, governing the expansion process, leads to deviations from the intended flow behaviour.

For the non-equilibrium case, Mach number as well as static and Pitot pressures most closely resemble the equilibrium case with  $\gamma_4 = 1.4$ , particularly with respect to the Mach number deficit at the nozzle axis. However, the boundary layer is 2.4 % thinner and the axial Mach number 2.9 % higher compared with the equilibrium counterpart. The thinner boundary layer in the non-equilibrium case is consistent with previous investigations of hypersonic boundary layers [31].

Figs. 7c and 7d further show that the flow in the divergent nozzle becomes frozen shortly after the throat, with a vibrational temperature of  $2100\,\mathrm{K}$  and an isentropic ratio of  $\gamma=1.3$ . The energy stored in vibrational modes is therefore unavailable for acceleration, resulting in a reduced axial velocity. Interestingly, this velocity corresponds best with the equilibrium case for  $\gamma_3 = 1.36$ , which is the nozzle design value. This indicates that, in terms of transforming stagnation enthalpy into kinetic energy, the original design choice of  $\gamma$  was appropriate.

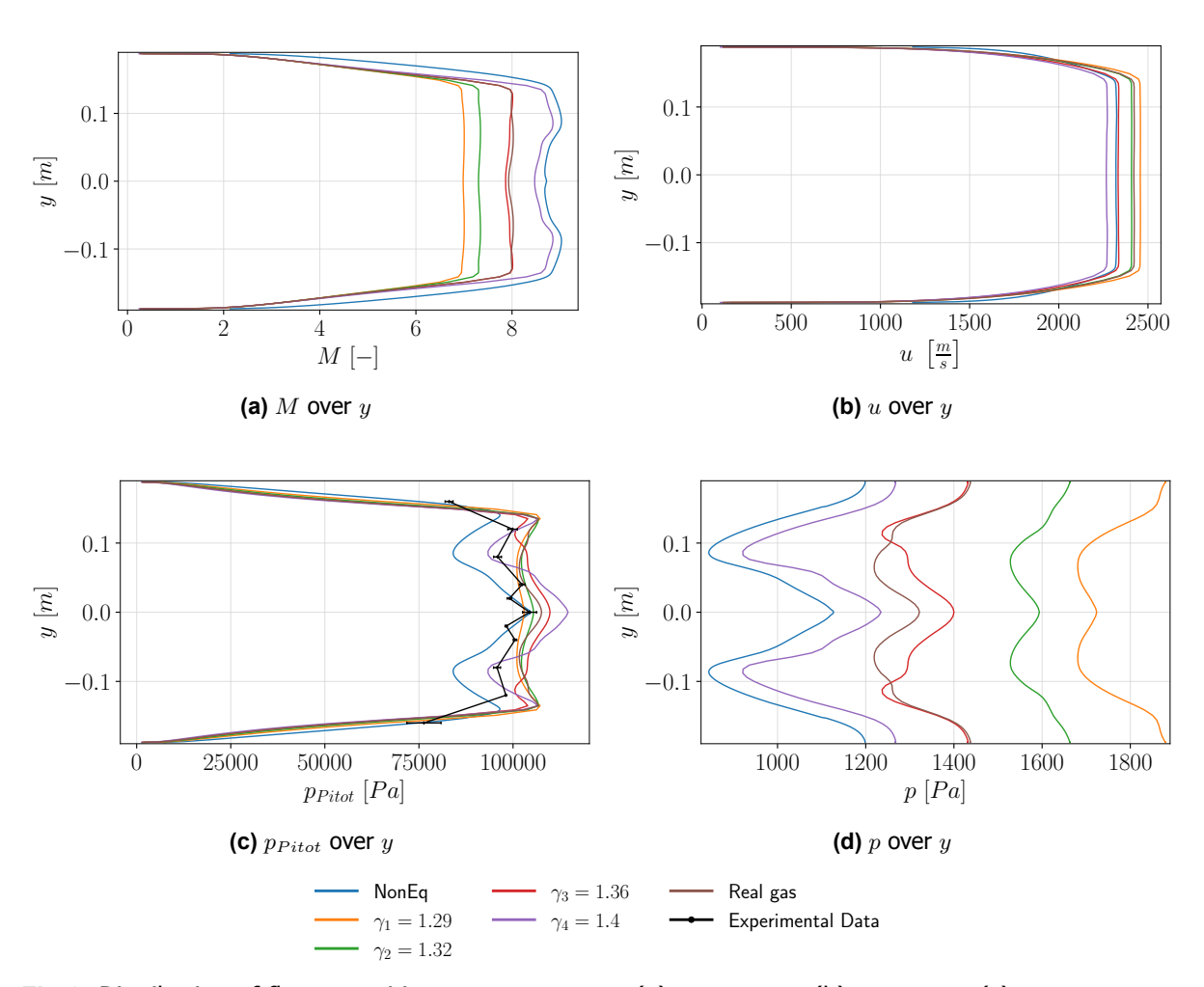


**Fig 6.** Distribution of flow quantities at  $x=-50\,\mathrm{mm}$ . (a): M over y; (b): u over y; (c):  $p_{Pitot}$  over y; (d): p over y

The real gas case shows good agreement with the  $\gamma_3=1.36$  equilibrium case in terms of Mach number, static pressure, and static temperature. Moreover, the overexpansion of the axial Mach number is less pronounced. This is attributed to the smaller effective  $\gamma$  in the expansion region, which produces shallower expansion waves. The reduced overexpansion is also evident in Fig 8e. In addition, the axial velocity at the nozzle exit corresponds most closely to the  $\gamma_2=1.32$  equilibrium case.

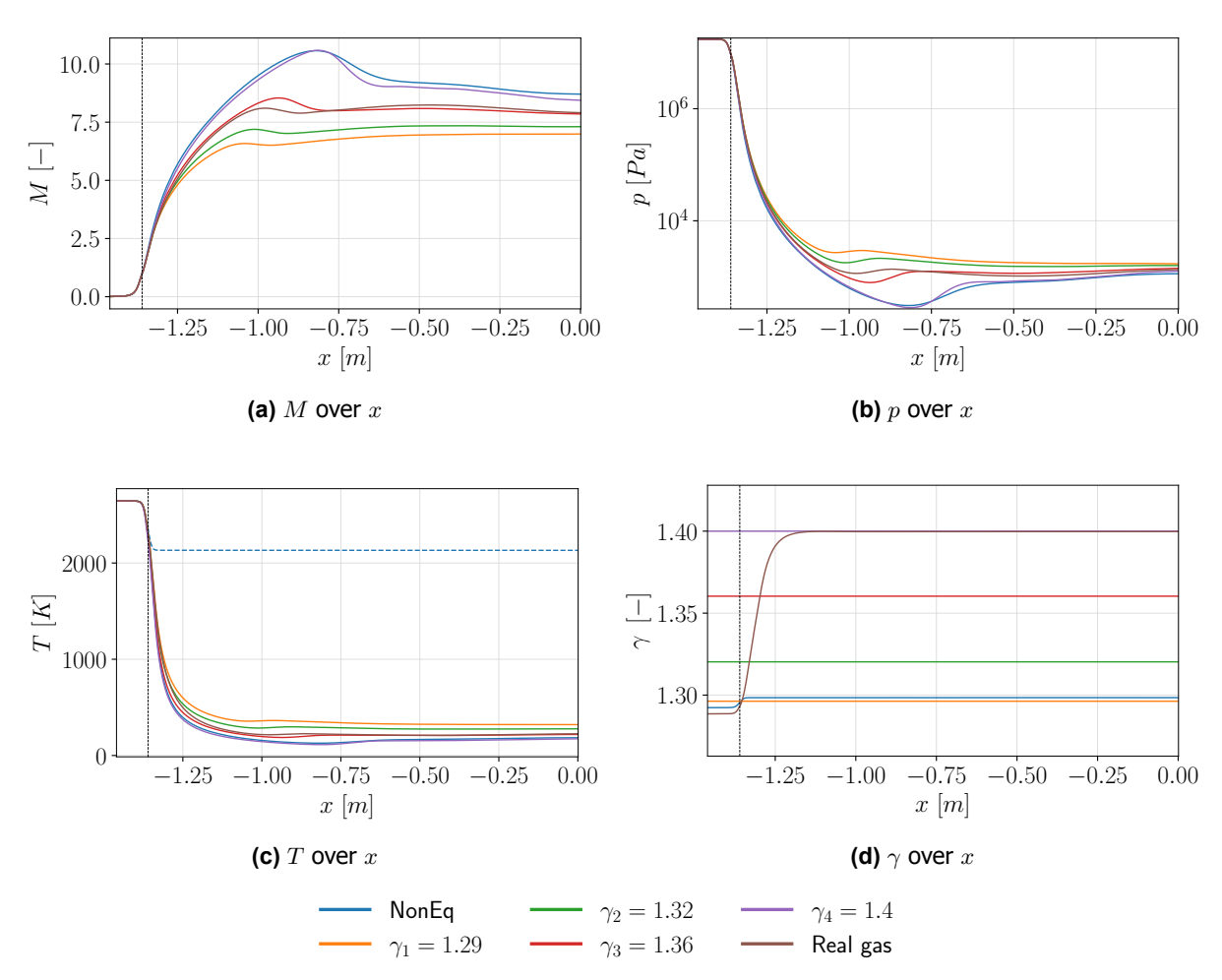


Fig 7. Flow quantities along nozzle centreline (y=0). The black dashed line denotes the position of the nozzle throat. (a): M over x; (b): p over x; (c): T over y with  $T_v$  for the non-equilibrium case as a dashed blue line; (d):  $\gamma$  over y;

Direct comparison with experimental Pitot pressure data (Fig 6c) shows a characteristic profile: a peak at the end of the boundary layer, a reduction towards the symmetry axis, and a secondary peak at the centreline. This behaviour becomes more pronounced with increasing  $\gamma$  in the equilibrium simulations. The non-equilibrium case again resembles the  $\gamma_4=1.4$  case qualitatively, but with Pitot pressures reduced by approximately  $1 \times 10^4 \, \text{Pa}$ . It matches the experimental data well at the nozzle centreline and boundary layer edge, but deviates in the intermediate region, where the equilibrium  $\gamma_4 = 1.4$  case provides the best agreement between the boundary layer and the centreline region.

For the nozzle contour optimization, the most important flow quantity is the Mach number. It is used in two objective functions and has to match best with the non-equilibrium results. This is the case for the perfect gas at  $\gamma = 1.4$ . Therefore, this value for  $\gamma$  is used for the optimization of the nozzle contour.

HiSST-2025-0057

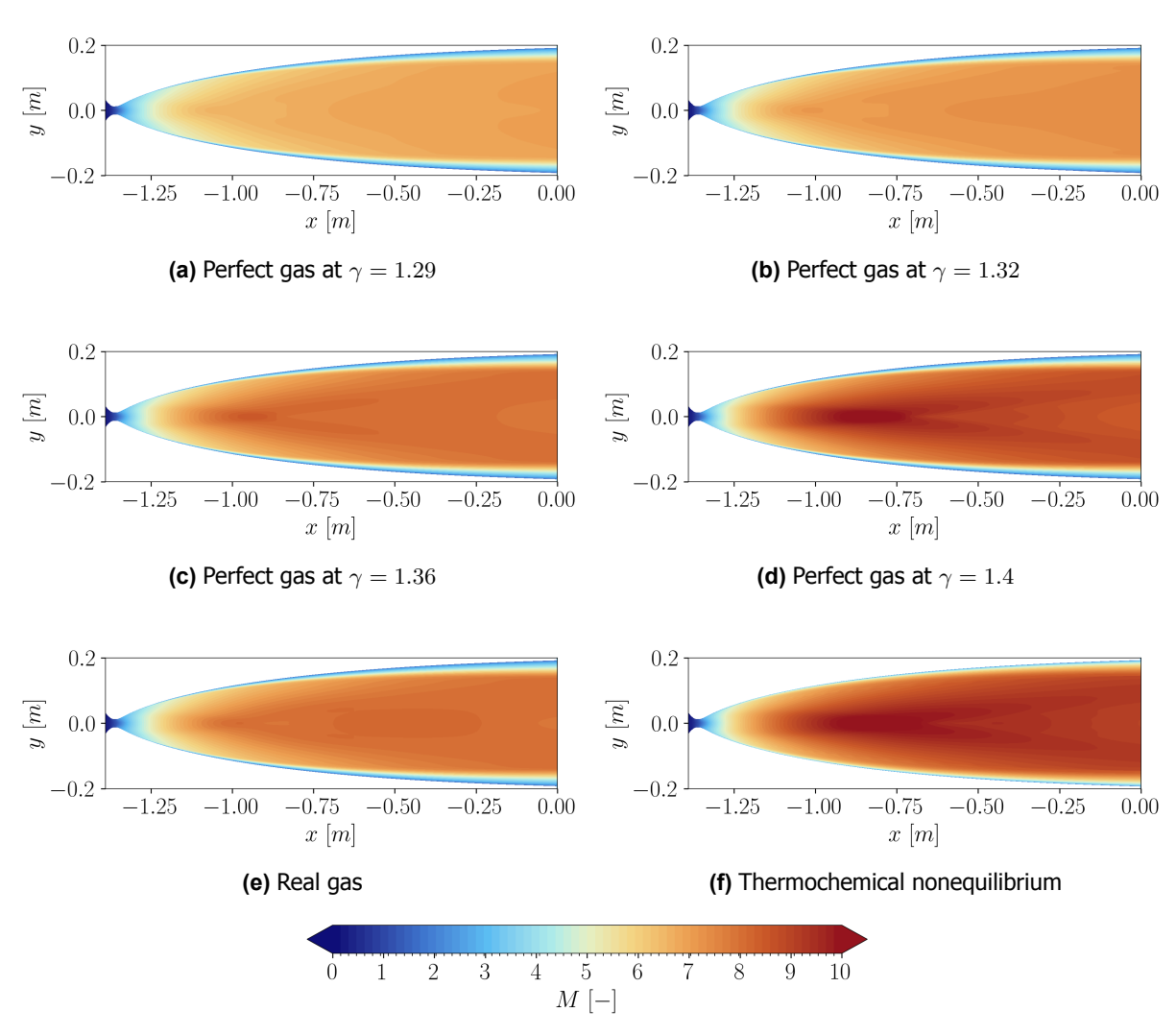


Fig 8. Mach number contour plot of nozzle flow. (a): perfect gas case with  $\gamma=1.29$ ; (b): perfect gas case with  $\gamma=1.32$ ; (c): perfect gas case with  $\gamma=1.36$ ; (d): perfect gas case with  $\gamma=1.4$ ; (e): real gas case; (f): non-equilibrium case

## 4.2. Nozzle Contour Optimisation

For all three objective combinations, a distinct Pareto front is observed, demonstrating the interdependence of the objectives and the absence of a unique global optimum, see Fig 9. Consequently, the results must be examined to determine which objective function should be prioritised; in this study, emphasis is placed on minimising the objective function associated with the nozzle exit Mach number profile when selecting the optimised contour.

With this prioritisation of  $M_e$ , solutions along the Pareto front were compared, revealing several systematic trends in the nozzle contour. A selection of representative geometries is shown in Fig 10 in three views: with equal aspect ratio, with the y-direction stretched, and with a close-up of the throat region.

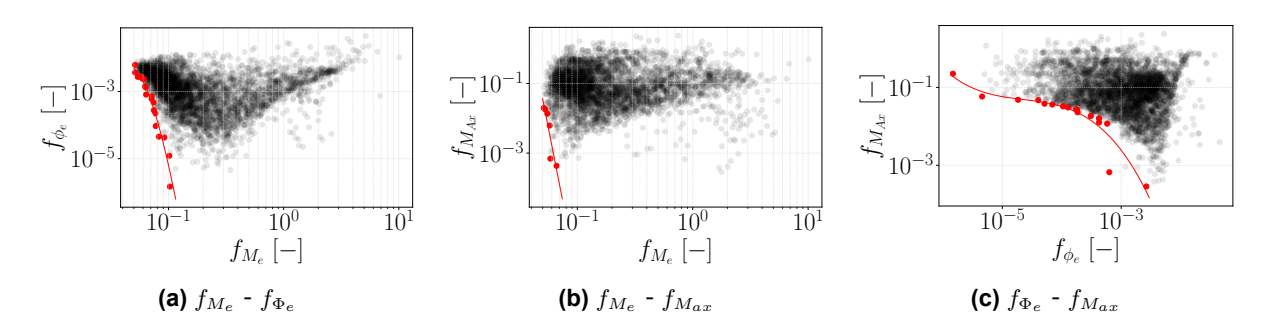


Fig 9. Objective function values from optimization. Black and grey points mark the results of the objective function for each simulation, red dots represent the Pareto-optimal points and the red lines are curve fits of the Pareto-optimal points. (a): Exit Mach number  $f_{M_e}$  and exit flow angle  $f_{\Phi_e}$ ; (b): exit Mach number  $f_{M_e}$  and centreline Mach number  $f_{M_{ax}}$ ; (c): exit flow angle  $f_{\Phi_e}$  and centreline Mach number  $f_{M_{ax}}$ .

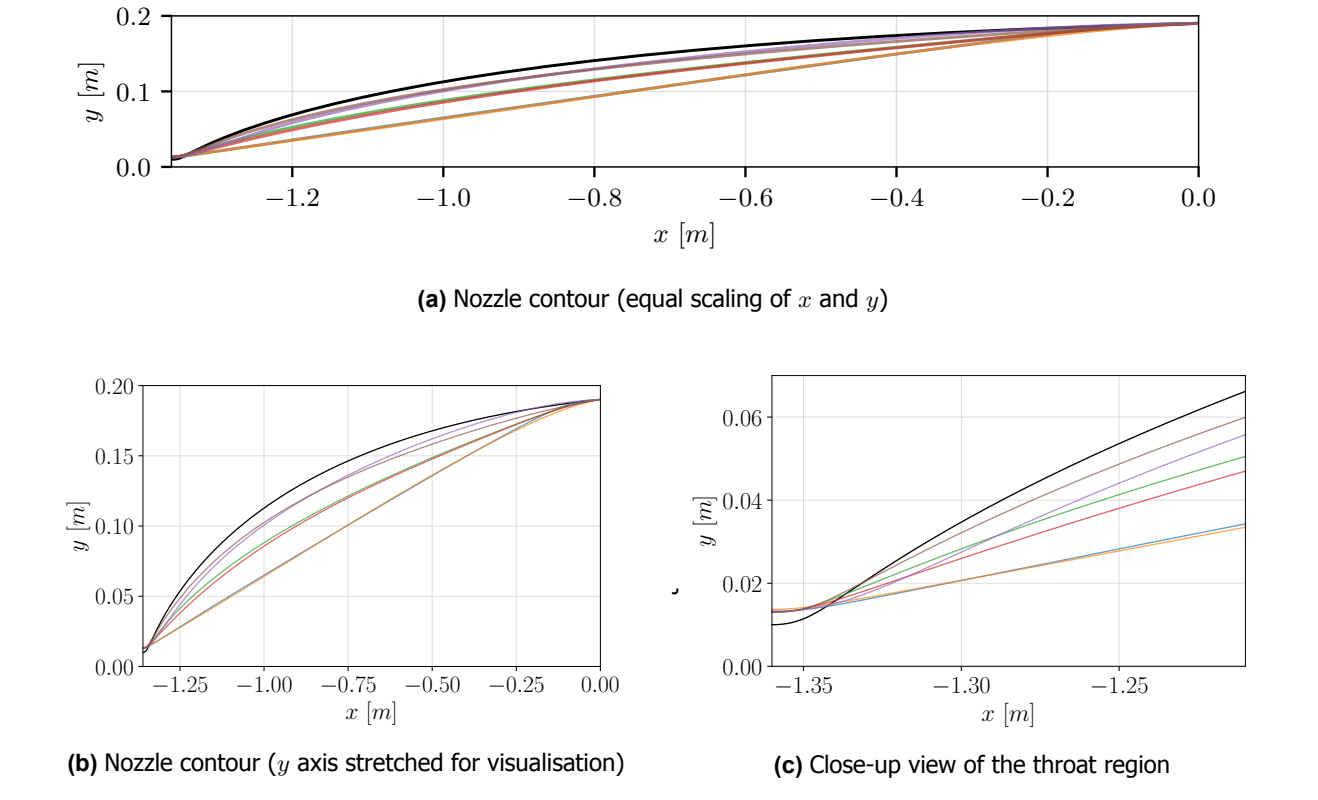


Fig 10. Comparison of initial and optimized nozzle contours in (a): equal aspect ratio representation; (b): stretched representation in y direction; (c): close-up of throat region

LC1

LC2

L1

Initial

C1

HiSST-2025-0057

Three distinct groups of solutions can be identified:

- i C (for conic),
- ii LC (for Laval conic),
- iii L (for Laval).

Group C contains contours resembling conical nozzles, while groups LC and L exhibit characteristics of classical bell-shaped nozzles. The distinction between LC and L lies in the wall angle at the inflection point: LC contours have a smaller angle and typically transition into a conical shape near the nozzle exit, whereas L contours have larger inflection angle and retain a closer resemblance to the initial contour throughout. A feature common to all groups is an increase of approximately  $30\,\%$  in throat radius compared with the initial contour. This enlargement results from the higher  $\gamma$  value used in the optimisation ( $\gamma=1.4$ ) relative to the original nozzle design ( $\gamma=1.36$ ), which reduces the required area ratio between throat and exit.

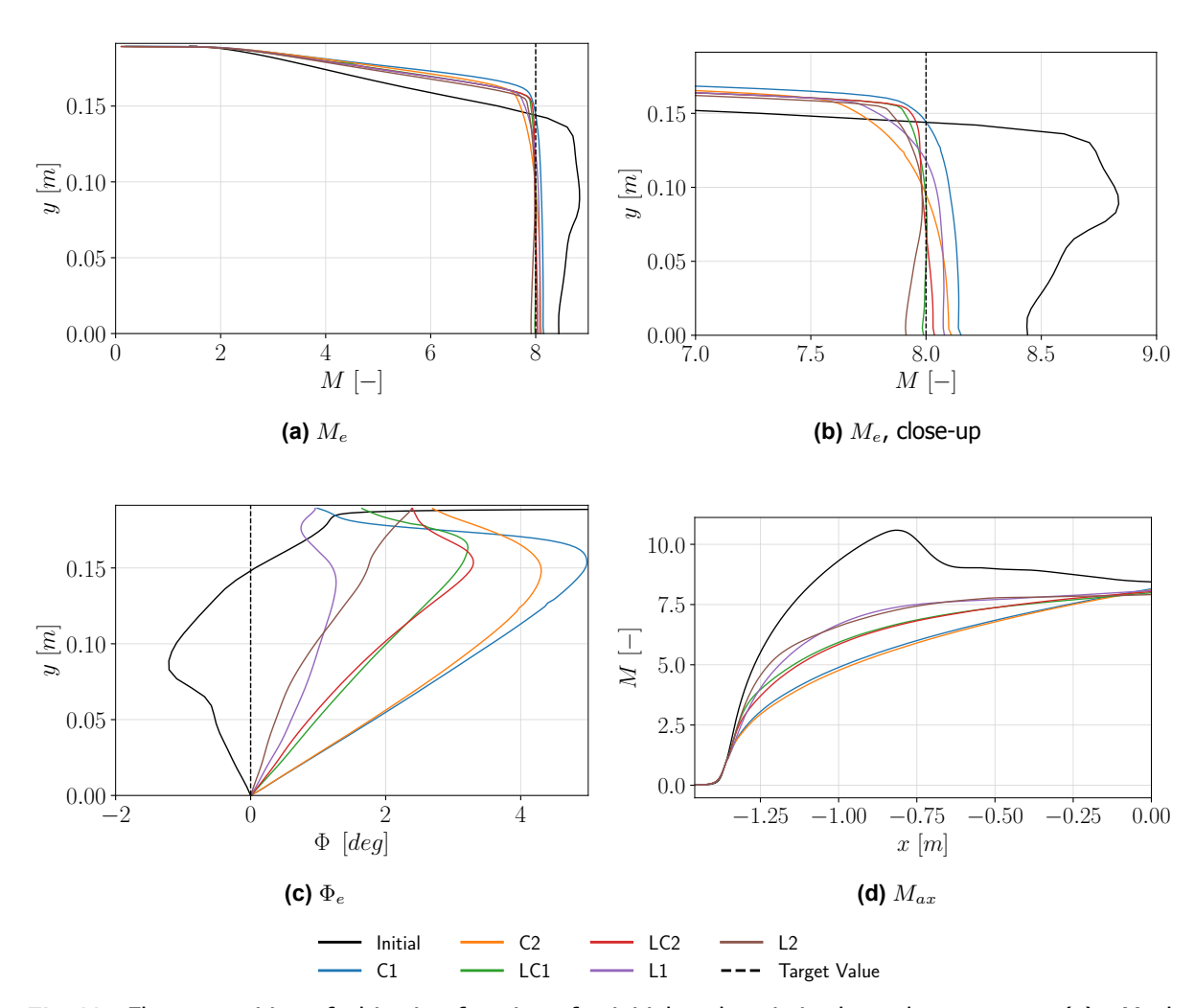


**Fig 11.** Flow quantities of objective functions for initial and optimized nozzle contours. (a): Mach number at nozzle exit; (b): Mach number at nozzle exit, close-up of Mach number around target value; (c): Flow angle at nozzle exit; (d): Mach number along centreline

The influence of the nozzle contour groups on the target values—namely the exit Mach number  $M_{e}$ , the flow angle  $\Phi_{e}$ , and the centreline Mach number  $M_{ax}$ —is presented in Fig 11. For  $M_{e}$ , all three

groups reproduce the target value of  $M_e=8$  more accurately than the initial contour, with a maximum deviation of only  $\Delta M_e=0.1$  at the axis of symmetry. Among the three, group LC shows the closest agreement with the target. All groups also exhibit a thinner boundary layer compared with the initial case, which can be attributed to the reduced arc length of the optimised contours.

For  $\Phi_e$ , group L demonstrates the smallest deviation, with the radial increase in flow angle remaining below that of the initial contour. In contrast, groups LC and C show a larger rise in  $\Phi_e$ , with group C reaching the highest values. In both cases, the maximum absolute value exceeds that of the initial contour. Within the boundary layer, however, the flow angle decreases. The progressive increase in  $\Phi_e$  from group L to LC to C is consistent with the growing proportion of conical sections in the corresponding contours.

A similar trend is noticeable for the centreline Mach number. Group L reaches the target value more rapidly and levels off earlier, while group LC follows a comparable trajectory but only stabilises close to the nozzle exit. Group C, in turn, continues to rise up to the exit. The distance required for  $M_{ax}$  to reach its target value correlates with the maximum wall angle: a shallower angle, whether at the inflection point (groups LC and L) or as the conical angle (group C), results in a shorter distance for  $M_{ax}$  to converge.

Besides the flow characteristics and structural loads, heat loads are a critical aspect in nozzle design and manufacturing. The total heat flux into the nozzle wall for the initial and optimised contours is shown in Fig 12. For all cases, the wall heat flux reaches its maximum at the throat and decreases towards the nozzle exit. Compared with the initial contour, the optimised nozzles exhibit reduced heat flux at the throat. Up to  $x=0.1\,\mathrm{m}$ , the heat flux of the initial contour as well as groups LC and L remains in a similar range, after which the optimised contours show a slower rate of decrease. Groups LC and L display similar qualitative trends, with group L consistently exhibiting lower heat flux than group LC. In contrast, contours from group C show higher heat flux along the entire arc length, though approaching the values of groups LC and L near the nozzle exit. Notably, in the exit region the wall heat flux of the optimised contours is two to three times higher than that of the initial nozzle.

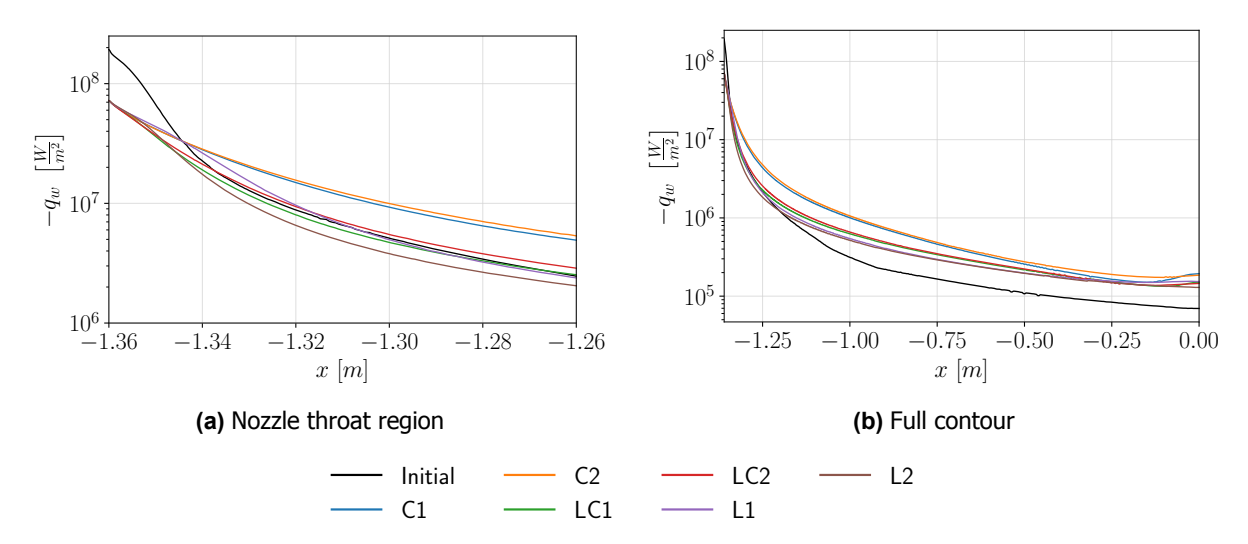
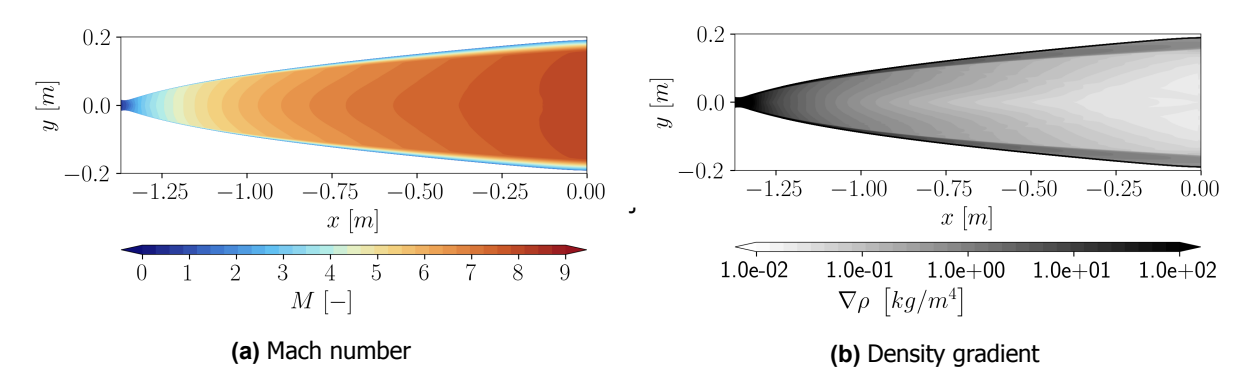


Fig 12. Logarithmically scaled wall heat flux  $q_w$  of initial and optimized nozzle contours. (a): nozzle throat region, (b): full contour

All three groups of optimised nozzle contours demonstrate clear improvements in flow characteristics compared with the initial design. However, prioritisation is required to determine which contour should be investigated further. The decisive criterion here is the deviation of the exit Mach number  $M_e$  from the target value. Taking into account both the requirements for the Mach number distribution at the nozzle exit and practical engineering and manufacturing considerations, contour LC1 is recommended.

For this configuration, the Mach number M and the density gradient  $\nabla \rho$  are illustrated in Fig 13.



**Fig 13.** Contour plots for (a) Mach number M and density gradient  $\nabla \rho$  of nozzle contour LC1

#### 5. Conclusion

In this study, a numerical evaluation of nozzle flows for the Mach 8 STB shock tube nozzle at flight conditions corresponding to  $H=30\,\mathrm{km}$  was performed. Three models were considered: perfect gas with varying  $\gamma$ , real gas, and thermochemical non-equilibrium.

The non-equilibrium simulations showed the closest agreement with experimental Pitot pressure data. However, the resulting exit Mach number  $M_e$  exceeded the target value of  $M_e=8$ . Among the equilibrium cases, the perfect gas model with  $\gamma=1.4$  exhibited the best agreement with the non-equilibrium results.

Based on these findings, a nozzle contour optimisation was conducted. Three distinct groups of optimised contours were identified: (i) conical nozzles, (ii) bell-shaped nozzles with a conical exit section, and (iii) bell-shaped nozzles, whereas the bell-shaped nozzle contours of group (ii) matches best with the target nozzle exit Mach number distribution.

Future work will focus on assessing the influence of different working gases and initial conditions on nozzle flow behaviour, particularly with respect to stronger thermochemical non-equilibrium effects at higher initial temperatures. In addition, the sensitivity of the flow to specific contour parameters, such as nozzle length, wall angle, and curvature, will be investigated in greater detail. Finally, the feasibility of modular nozzle concepts will be explored.

In summary, the study demonstrates the successful integration of gas model evaluation with systematic contour optimisation, yielding enhanced nozzle performance under hypersonic flow conditions.

# Acknowledgment

The authors gratefully acknowledge the Federal High Performance Computing Center Stuttgart (HLRS) for providing the computational resources on NEC Cluster 'Vulcan'.

#### References

- [1] B. Sauerwein, R. Hruschka, P. Gnemmi, C. Rey, and M. Bastide, *ISL Shock Tunnel Operation with Contoured Mach-4.5-6-8-10-Nozzles for Hypersonic Test Applications*. 2015.
- [2] L. Prandtl and A. Busemann, *Näherungsverfahren zur zeichnerischen Ermittlung von ebenen Strömungen mit Überschallgeschwindigkeit.* Zürich, Switzerland: Füssli Verlag, 1929.
- [3] K. Foelsch, "The analytical design of an axially symmetric laval nozzle for a parallel and uniform jet," *Journal of the Aeronautical Sciences*, vol. 16, no. 3, pp. 161–166, 1949.
- [4] J. C. Sivells, "Aerodynamic design of axisymmetric hypersonic wind-tunnel nozzles," *Journal of Spacecraft and Rockets*, vol. 7, pp. 1292–1299, 1970.

- [5] J. Benton, A. Edwards, and J. Perkins, "Limitations of the method of characteristics when applied to axisymmetric hypersonic nozzle design," 28th Aerospace Sciences Meeting, 1990, 1990.
- [6] G. Candler and J. Perkins, Effects of vibrational nonequilibrium on axisymmetric hypersonic nozzle design. 1991.
- [7] Y. Wang and Z. Jiang, "Theories and methods for designing hypersonic high-enthalpy flow nozzles," *Chinese Journal of Aeronautics*, vol. 35, pp. 318–339, 1 2022.
- [8] J. Korte, A. Kumar, D. Singh, and J. White, "CAN-DO, CFD-based Aerodynamic Nozzle Design and Optimization Program for Supersonic/hypersonic wind tunnels," AIAA 17th Aerospace Ground Testing Conference, 1992, 1992.
- [9] M. Matsunaga, C. Fujio, H. Ogawa, Y. Higa, and T. Handa, "Nozzle design optimization for supersonic wind tunnel by using surrogate-assisted evolutionary algorithms," *Aerospace Science and Technology*, vol. 130, 2022.
- [10] Y. Wang, Q. Eri, J. Huang, and B. Kong, "Multi-objective aerodynamic optimization of expansion—deflection nozzle based on b-spline curves," *Aerospace Science and Technology*, vol. 147, 2024.
- [11] D. E. Goldberg, "Genetic algorithms in search, optimization, and machine learning, addison-wesley, reading, ma, 1989," NN Schraudolph and J.., vol. 3, 1989.
- [12] H. G. Weller, G. Tabor, H. Jasak, and C. Fureby, "A tensorial approach to computational continuum mechanics using object-oriented techniques," *Computers in Physics*, vol. 12, no. 6, 1998.
- [13] J. Heyns, O. F. Oxtoby, and A. Steenkamp, "Modelling high-speed viscous flow in openfoam® modelling high-speed flow using a matrix-free coupled solver," 2014.
- [14] B. Adams, W. Bohnhoff, K. Dalbey, M. S. Ebeida, J. P. Eddy, M. S. Eldred, R. W. Hopper, P. Hough, K. Hu, J. Jakeman, M. Khalil, K. Maupin, J. Monschke, E. Prudencio, E. Ridgway, P. Robbe, A. Rushdi, D. Seidl, J. Stephens, L. Swiler, and J. Winokur, "Dakota 6.19.0 documentation.," Tech. Rep. SAND2023-13392O, Sandia National Laboratories, 11 2023.
- [15] J. C. Sivells, "A computer program for the aerodynamic design of axisymmetric and planar nozzles for supersonic and hypersonic wind tunnels.," Tech. Rep. AEDC-TR-78-63, Arnold Engineering Development Center, 1978.
- [16] R. Tolle, "A new optimum design code for hypersonic nozzles, utilizing response surface methodology," 35th Aerospace Sciences Meeting and Exhibit, 1997.
- [17] W. Zhang, Z. Zhang, X. Wang, and T. Su, "A review of the mathematical modeling of equilibrium and nonequilibrium hypersonic flows," 2022.
- [18] International Organization for Standardization (ISO), "Standard atmosphere," 1975.
- [19] J. L. Strolley, J. E. Smith, and C. Park, "The effects of vibrational relaxation on hypersonic nozzle flows," in *The High Temperature Aspects of Hypersonic Flow* (W. C. Nelson, ed.), vol. 68, pp. 49–66, NATO, Advisory Group for Aeronautical Research and Development, 1964.
- [20] C. Park, Nonequilibrium Hypersonic Aerothermodynamics, vol. 44. Wiley International, 1990.
- [21] L. Landau and E. Teller, "Zur theorie der schalldispersion," Physikalische Zeitschrift der Sowjetunion, vol. 10, no. 1, p. 34, 1936.
- [22] V. Casseau, R. C. Palharini, T. J. Scanlon, and R. E. Brown, "A two-temperature open-source cfd model for hypersonic reacting flows, part one: Zero-dimensional analysis," *Aerospace*, vol. 3, pp. 1–21, 2016.
- [23] V. Casseau, D. E. Espinoza, T. J. Scanlon, and R. E. Brown, "A two-temperature open-source cfd model for hypersonic reacting flows, part two: Multi-dimensional analysis," *Aerospace*, vol. 3, 2016.

- [24] R. J. Gollan and P. A. Jacobs, "About the formulation, verification and validation of the hypersonic flow solver eilmer," *International Journal for Numerical Methods in Fluids*, vol. 73, 2013.
- [25] N. N. Gibbons, K. A. Damm, P. A. Jacobs, and R. J. Gollan, "Eilmer: An open-source multi-physics hypersonic flow solver," *Computer Physics Communications*, vol. 282, 2023.
- [26] P. Spalart and S. Allmaras, A one-equation turbulence model for aerodynamic flows. 1992.
- [27] D.-Y. Peng and D. B. Robinson, "A new two-constant equation of state," *Industrial & Engineering Chemistry Fundamentals*, vol. 15, no. 1, pp. 59–64, 1976.
- [28] M. Chase, NIST-JANAF Thermochemical Tables, 4th Edition. American Institute of Physics, -1, 1998-08-01 1998.
- [29] C. Park, "Review of chemical-kinetic problems of future nasa missions, i: Earth entries," *Journal of Thermophysics and Heat Transfer*, vol. 7, pp. 385–398, 1993.
- [30] R. C. Millikan and D. R. White, "Systematics of vibrational relaxation," *The Journal of Chemical Physics*, vol. 39, pp. 3209–3123, 12 1963.
- [31] D. Passiatore, L. Sciacovelli, P. Cinnella, and G. Pascazio, "Thermochemical non-equilibrium effects in turbulent hypersonic boundary layers," *Journal of Fluid Mechanics*, vol. 941, p. A21, 2022.